# University of Groningen

## Amorphous AlN films grown by ALD from trimethylaluminum and monomethylhydrazine

Parkhomenko, Roman G.; De Luca, Oreste; Kołodziejczyk, Łukasz; Modin, Evgeny; Rudolf, Petra; Martínez Martínez, Diego; Cunha, Luis; Knez, Mato

**IMPORTANT NOTE: You are advised to consult the publisher's version (publisher's PDF) if you wish to cite from it. Please check the document version below.**

*Document Version*
Publisher's PDF, also known as Version of record

[Link to publication in University of Groningen/UMCG research database](#)

Check for updates

# Amorphous AlN films grown by ALD from trimethylaluminum and monomethylhydrazine

Roman G. Parkhomenko, [ID] *[a] Oreste De Luca, [ID] [b] Łukasz Kołodziejczyk, [ID] [c] Evgeny Modin,[a] Petra Rudolf, [ID] [b] Diego Martínez Martínez, [ID] [d] Luis Cunha[d] and Mato Knez [ID] [a,e]

The great interest in aluminium nitride thin films has been attributed to their excellent dielectric, thermal and mechanical properties. Here we present the results of amorphous AlN films obtained by atomic layer deposition. We used trimethylaluminum and monomethylhydrazine as the precursors at a deposition temperature of 375–475 °C. The structural and mechanical properties and chemical composition of the synthesized films were investigated in detail by X-ray diffraction, X-ray photoelectron spectroscopy, electron and probe microscopy and nanoindentation. The obtained films were compact and continuous, exhibiting amorphous nature with homogeneous in-depth composition, at an oxygen content of as low as 4 at%. The mechanical properties were comparable to those of AlN films produced by other techniques.

## Introduction

Aluminium nitride thin films have gained attention due to their excellent electrical and mechanical properties, namely, their wide bandgap, good piezoelectric response, high resistance to bending, and remarkable thermal and chemical stability, and their optical properties; consequently they found application in sensors, light-emitting diodes, or as insulating layers.[1–8] Emerging devices of great interest are high electron mobility transistors, where AlN layers are used as buffer layers for GaN films to compensate for the misfit of the lattices and the thermal expansion between the substrate and GaN.[9,10]

AlN thin films have been deposited using various chemical and physical methods, including metal organic vapor phase epitaxy, ion-beam deposition and magnetron sputtering.[11–13] Despite their wide use, all these methods have drawbacks, which hamper their industrial exploitation. For example, the films must show good uniformity and conformality throughout the entire surface to be covered. Another important point is that the film thickness must be controlled at the Angstrom level. The method of choice that meets all these criteria is

atomic layer deposition (ALD) because it relies on the self-saturating exposure of substrates to vaporized precursors. The precursors are introduced into a reactor alternately, resulting in self-limiting film growth that allows one to achieve atomic scale thickness control with excellent conformality. Amorphous AlN films are of particular interest due to their improved mechanical, electrical and optical properties compared to those of the crystalline phase of AlN.[14–17] However, most AlN films grown by ALD are of crystalline nature[18–25] hence obtaining amorphous AlN films by ALD is an actual problem. $AlCl_3$ with $NH_3$ is a common precursor combination that has often been used for depositing AlN.[26,27] However, the use of $AlCl_3$ leads to substantial chlorine contamination in the films due to the evolution of HCl as the by-product, which also causes severe corrosion of reactor components over time. An alternative precursor that is widely used as the Al source is trimethylaluminum (TMA) but it is rarely considered in combination with ammonia due to its low decomposition temperature. In fact, the growth of AlN films with ammonia by ALD requires substantial energy input, since $NH_3$ exhibits a low affinity to the growing surfaces owing to the strong N–H bond (389 kJ mol$^{-1}$). Hence, plasma processes are often used instead to lower the thermal budget.[21–26] However, not all ALD reactors have plasma units. Moreover, a huge fraction of reactors in use worldwide is not suitable for a plasma upgrade from an engineering standpoint, which is a considerable obstacle for many research groups. To avoid the use of plasma, the corrosion of the reactor by HCl, and/or the contamination of the AlN films with chlorine, the use of TMA in combination with a highly reactive nitrogen source is desired. Monomethylhydrazine (MMH) is a more reactive precursor

*[a]CIC NanoGUNE, Tolosa Hiribidea 76, E-20018 San Sebastian, Spain.
E-mail: r.parkhomenko@nanogune.eu
[b]Zernike Institute for Advanced Materials, University of Groningen, Nijenborgh 4, 9747 AG Groningen, The Netherlands
[c]Institute of Materials Science and Engineering, Lodz University of Technology, Stefanowskiego 1/15, 90-924 Lodz, Poland
[d]Physics Center of Minho and Porto Universities-CF-UM-UP, School of Sciences, University of Minho, Campus de Gualtar, 4710-057 Braga, Portugal
[e]IKERBASQUE, Basque Foundation for Science, Alameda Urquijo 36-5, 48011 Bilbao, Spain*

that fulfils those criteria. Hydrazine derivatives have already been used for the deposition of transition metals by ALD,[28] but AlN processes have not been studied to date. Here, we perform an investigation of amorphous AlN films grown by ALD from TMA and MMH, where we determined their composition, structure, morphological features, and their mechanical properties and demonstrate that the use of MMH leads to the formation of high quality AlN films with good uniformity.

## Experimental section

ALD experiments were carried out in a semi-industrial, commercial ALD reactor (Beneq TFS-200). Trimethylaluminum (98%, Strem Chemicals) and monomethylhydrazine (98%, Sigma-Aldrich) were supplied at their own vapor pressure, without additional heating. The reactor was heated to temperatures between 375 and 475 °C. Nitrogen (99.99%, Nippon Gases) was used as a carrier gas at 200 sccm and continuously delivered through the precursor manifold. The AlN films were deposited on Si(100) substrates (PI-KEM Ltd) with a size of 10 × 10 mm with a terminal native oxide thickness of ~2 nm in a reactor with a diameter of 200 mm. For each run we positioned a multitude of substrates in the chamber to evaluate the uniformity. The samples were placed in the centre of the reactor and radially around the reactor perimeter. We did not observe any difference in neither the composition, nor the thickness or morphology. A typical ALD process consisted of 0.1 s TMA pulse → 2 s purge with $N_2$ → 0.1 s MMH pulse → 2 s purge with $N_2$ and the pressure in the reactor was 67 Pa in all experiments. Scanning electron microscopy (SEM) images of the films were obtained with a Helios NanoLab 450S microscope (FEI, The Netherlands) at an accelerating voltage of 1–5 kV and a beam current of 13 pA. The sample preparation for transmission electron microscopy (TEM) imaging was performed on a FIB/SEM machine Helios Nanolab 450S (FEI, The Netherlands). We used the normal protocol of the FIB lift-out procedure to prepare the cross-section: the region of interest was locally covered with the protective layer of platinum and then extracted from the bulk with the micromanipulator. Furthermore, it was attached to the TEM lift-out grid and thinned down to the electron transparency. TEM measurements were performed using a Titan 60–300 (FEI, The Netherlands) equipment operated at an accelerating voltage of 300 kV. X-ray diffraction (XRD) and X-ray reflectivity (XRR) measurements were performed using a Panalytical X'PertPRO diffractometer with Cu Kα radiation (40 kV, 40 mA). XRD patterns were recorded in the $2\theta$ range from 10 to 80°, in steps of 0.015° and with a counting time of 8 s per step in a grazing incidence configuration with grazing angles of 0.5–2°. XRR patterns (for thickness determination) were recorded in the $2\theta$ range from 0.1 to 2°, in steps of 0.008° and with a counting time of 2 s per step. X-ray photoelectron spectroscopy (XPS) was conducted using a Surface Science SSX-100 ESCA spectrometer with a monochromatic Al Kα X-ray source ($h\nu$ = 1486.6 eV). The pressure in the measurement chamber was main-

tained below $1 \times 10^{-7}$ Pa during data acquisition; the electron take-off angle with respect to the surface normal was 37°. The XPS data were acquired on a spot of 1000 µm diameter and the energy resolution was set to 1.3 eV for both the survey spectra and the detailed spectra of the Al 2p, C 1s, N 1s and O 1s core level regions. Binding energies are reported to be ±0.1 eV and referenced to the Al 2p photoemission peak (Al–N species) centred at a binding energy of 74.3 eV.[29] All XPS spectra were analysed using the least-squares curve-fitting program Winspec (LISE laboratory, University of Namur, Belgium). The deconvolution of the spectra included a Shirley baseline subtraction and fitting with a minimum number of peaks consistent with the composition of the thin film, taking into account the experimental resolution. The profile of the peaks was taken as a convolution of Gaussian and Lorentzian functions. The uncertainty in the peak intensity determination was within 2% for all core levels reported. XPS depth profiling was conducted by alternating Argon sputtering at 5 keV, and optimized to minimize the preferential sputtering of elements. The sputtering rate of ~3 ± 1 nm per hour was determined from the sputtered depth, measured using stylus profilometry, and sputtering time. Spectra were acquired on two distinct spots for each of the indicated sputtering times.

Surface morphology and topography analysis were performed under ambient conditions using a Multimode 5 atomic force microscope (AFM) equipped with a Nanoscope V controller (Bruker Corporation). AFM measurements were repeated three times on different reference areas. Topography measurements were performed in the tapping mode and the sizes of the images were 1 × 1 µm and 5 × 5 µm. Commercial silicon probes of type OTESPA (MicroMasch), with a tetrahedral shape with a nominal tip radius < 7 nm were used for optimized positioning on the sample; the cantilever spring constant was 26 N m$^{-1}$ and the resonant frequency was 300 kHz. Image acquisition was performed using the Nanoscope 7.3 software and further image processing was done using the Nanoscope Analysis 1.9 (Bruker Corporation) and MountainsMap Premium 5.0 (Digital Surf) software. Commonly known geometric surface structure parameters of the samples, average roughness ($R_a$), maximum roughness ($R_z$) and root-mean square roughness (RMS), were defined as average values taken from 1024 surface profiles based on images with a scan size of 10 × 10 µm. The error was calculated as the standard deviation among all surface profiles. The size of the globular domains of AlN coating was calculated using the SPIP 6 image processing software (Image Metrology A/S). The prepared topography images were processed using the Pore and Particle analysis option in the Watershed – Packed Features segmentation mode (this method is used when the image is fully covered by adjoining features of the same type with no spacing in between).

Hardness and elastic modulus of the coatings were measured using the nanoindentation technique on a Nano Indenter G200 system (KLA Corporation). For nanoindentation a diamond Berkovich tip (Micro Star Technologies) and the continuous stiffness measurement mode were used. The tip shape was calibrated by conducting experiments on a fused silica standard and the data were analysed using the Oliver

and Pharr approach.[30] 25 experiments were performed on the AlN sample at a strain rate of 0.05 s$^{-1}$, a harmonic displacement of 2 nm and a frequency of 45 Hz. In order to obtain the real values of mechanical properties with a minimized substrate effect on the result, thus leading to higher convergence of the obtained result with the actual value, samples with thicker AlN coating (370 nm) were selected. The used Poisson ratio of the AlN films was 0.25.[31] In addition, the obtained values were supplemented with the results measured for the bare Si substrate. For adhesion strength measurements a diamond cone with an apex angle of 90° and a radius of 1 μm was used. The delamination force was determined based on the friction coefficient evolution and penetration depth changes registered during the measurement process. The normal load increased linearly at a 0.2 mN μm$^{-1}$ rate and the scratch velocity was 1 μm s$^{-1}$. Eight nanoscratch experiments were performed on each AlN sample. Nano-wear tests were conducted in reciprocating the sliding mode with the use of a nanoindenter equipped with a diamond conical tip with 1 μm radius and an apex angle of 90°. The tests were carried out for 500 cycles at low normal forces ranging from 3 mN to 10 mN, a sliding distance and frequency of 50 μm and 0.5 Hz, respectively. All tests were performed under ambient conditions. Six experiments for each value of selected normal force were conducted on each sample. Cross profile measurements in the location of the wear tests allowed specific wear coefficient calculations, based on the Archard equation.[32]

## Results and discussion

### Film growth

The deposition of AlN films from TMA and MMG comprised alternately pulsing the precursors with purging after each pulse. To obtain detailed information about the ALD process, the growth of the films was studied for different growth parameters, i.e. different pulse duration of the precursors, purge time and temperature of the reactor. The deposition experiments were performed in a range from 375 to 475 °C. With increasing deposition temperature the growth per cycle (GPC) increased linearly from 0.66 to 1.34 Å per cycle (Fig. 1a). Recently, Kim et al. obtained a substantially higher GPC, namely >3 Å per cycle at 350 °C when using TMA and N$_2$H$_4$.[33] In view of the overall higher reactivity of hydrazine derivatives compared to that of hydrazine an increase in the GPC was expected for MMH; however, in our experiments we were unable to reach their values. It is known that hydrazine methyl-derivatives decompose at 200–300 °C through a radical formation mechanism. At an initiation stage the energy needed to break the N–N bond of MMH is higher than that of hydrazine. However, the methyl substituent provides a source of methyl radicals facilitating and enhancing the chain effect, which results in a higher overall decomposition rate of the MMH and the formation of less reactive species in the gas phase, such as NH$_3$ and N$_2$. Therefore, the lower growth rate of the AlN films in the present work can be explained by the competing reactions occurring in the gas phase. In addition, it was shown that the presence of water, even in a small amount, can substantially (up to 10 times) lower the reactivity of hydrazine derivatives.[34] In our case, MMH containing up to 2% of water was used, which potentially contributed to the lower GPC. We also explored the change in the GPC with pulse time and found that with increasing pulse time of MMH (0.2 s), the GPC remained almost the same, as it is expected from an ideal ALD process. An extension of the TMA pulse time (0.2 s) did not lead to an increased GPC neither. Purge time variation between 1 and 3 s did not affect the growth rate. It should be noted that even though our experiments were performed at
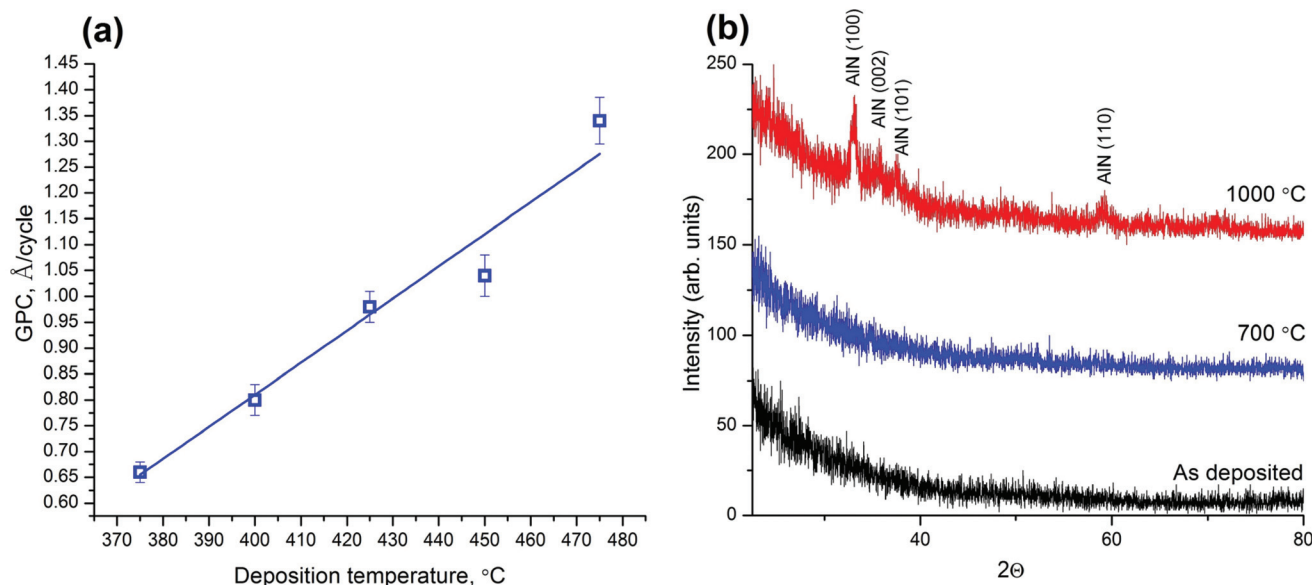


Fig. 1 (a) Growth per cycle as a function of the deposition temperature; (b) XRD patterns of AlN films annealed at different temperatures.

temperatures above the decomposition temperatures of the precursors, the decomposition seems to not affect the processes on the surface or only very weakly affect them, otherwise an enhanced growth would have been observed upon increasing the pulsing time of the precursors (and thereby the exposure time). As a partial decomposition will be unavoidable at those temperatures, we believe that the decomposition occurs in the gas phase only and potentially generates volatile byproducts, which do not affect the film growth.

The XRD analysis (Fig. 1b) shows that all as-deposited films showed no peaks in the patterns indicating an amorphous structure. At the same time the HR-TEM micrographs (Fig. 2b) indicate that the films are not amorphous in the classical sense, since they are composed of very small nanocrystallites with a distorted lattice embedded in an amorphous matrix. These nanocrystallites are not resolved by XRD, which may be due to their small sizes and/or the ratio of the crystalline to amorphous fraction. In this respect, we have to clarify that we do not grow fully amorphous AlN films but suppress to some extent the crystallite formation in the amorphous AlN. Crystallinity generally increases with the deposition temperature, however according to the literature most of the AlN films grown both at relatively low and high temperatures are crystalline.[18–25] This fact indicates that the major contributing factor leading to a decrease in the crystallinity is apparently not the deposition temperature but the chemical structure of
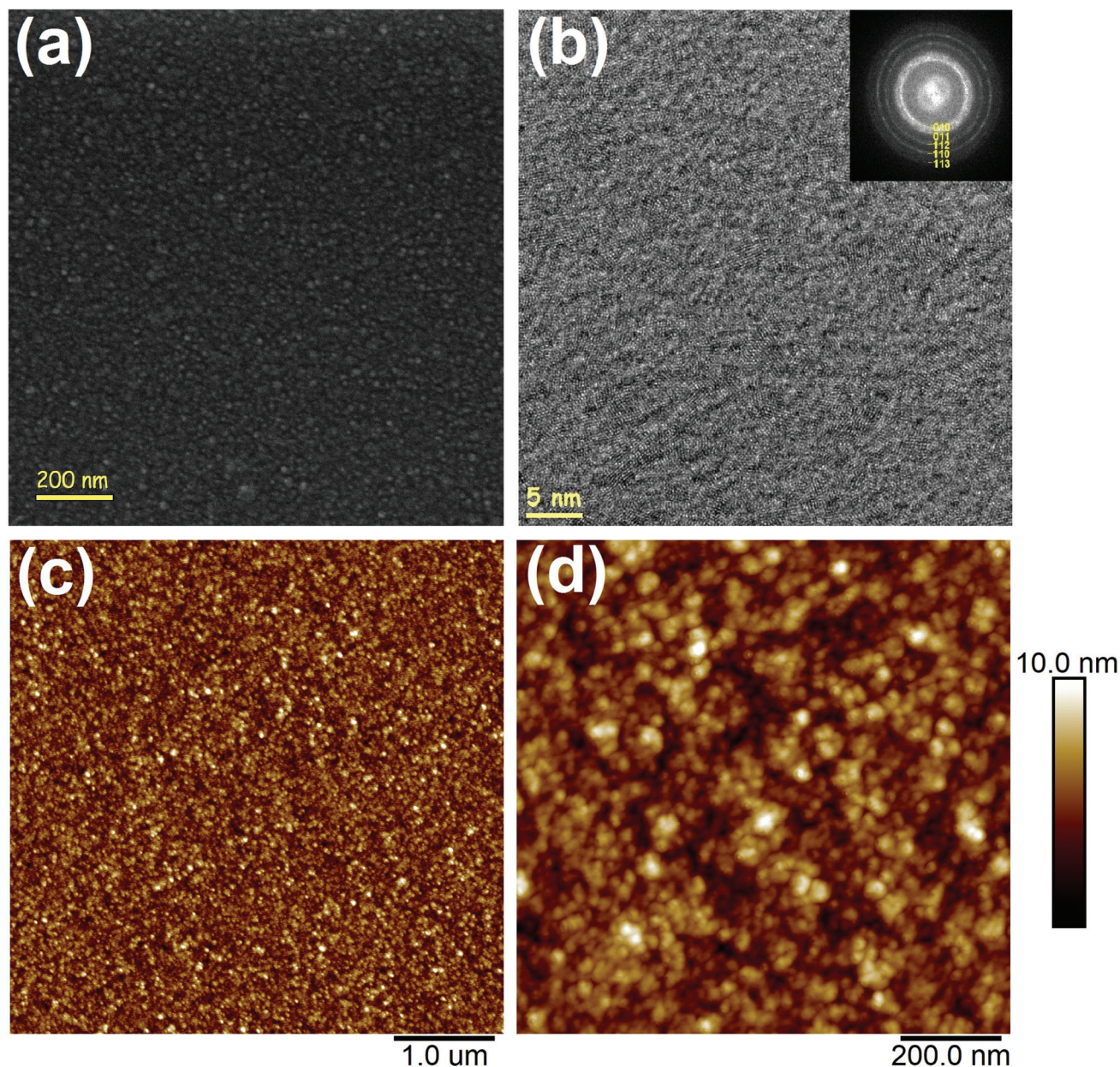


Fig. 2   (a) SEM, (b) TEM and (c and d) AFM images of an AlN film grown at 450 °C.

MMH. Namely, the suppression in crystallinity is likely resulting from the presence of methyl groups in the MMH molecules, which upon reaction at the surface occupy more space than $NH_3$ or $N_2H_4$, thereby disturbing the order and suppressing the crystallite growth. With this hypothesis we can assume that the use of higher substituted hydrazine derivatives, for example, unsymmetrical dimethylhydrazine or *tert*-butylhydrazine, might further decrease the crystallinity. Annealing at a temperature of 700 °C for 2 hours in a nitrogen atmosphere did not change the XRD patterns. However, at 1000 °C an onset in crystal formation was observed.

## Morphology

For detailed investigations we chose the films deposited in the center of the studied deposition temperature range (450 °C). Fig. 2a and b show the typical top view SEM and TEM images of the AlN film surface. The films consist of agglomerates with an average grain size of 9–15 nm. The circles in the FFT image (inset in Fig. 2b) correspond well to the appropriate lattice spacing of AlN.

According to the AFM data, the surface of the coating is compact and continuous. The investigated films show a granular structure with a relatively smooth surface (Fig. 2c and d) and uniform grain size with an RMS roughness of $1.40 \pm 0.13$ nm ($R_z = 7.95 \pm 1.07$ nm, $R_a = 1.10 \pm 0.09$ nm). There are neither voids between the grains, nor conglomerates of considerable size, as reflected by the small values of standard deviation of the coatings' roughness parameters. The estimated grain size from the AFM images is $14.7 \pm 4.4$ nm, which agrees with the SEM results.

## Chemical composition

An XPS depth profile analysis over the entire thickness of the sample was performed to investigate the chemical composition of the AlN film deposited at 450 °C. The XPS survey spectra and the stoichiometric analysis, as deduced from the XPS depth profile, are shown in Fig. 3. The sputtered depth corresponds to the fraction of the AlN film removed after each sputtering cycle. A depth of about 3 nm is obtained after 1 hour of $Ar^+$ sputtering.

Before $Ar^+$ sputtering, the most noteworthy features in the XPS survey spectrum are the carbon and oxygen peaks. Indeed, it is well known that the substrates with an aluminium nitride coating oxidize in air, forming a passivating alumina film.[35,36] Besides, exposure to air between ALD deposition and XPS analysis leads to contamination of the film surface. A small signature of chlorine (~0.5 at%) is also present on the surface.

Upon sputtering, both the aluminium and nitrogen contributions increased rapidly with the depth, while the carbon and oxygen contents decreased significantly (Fig. 4). The AlN film became quasi-stoichiometric after 4 h of $Ar^+$ sputtering (*i.e.* at a depth of ~12 nm); the concentrations of aluminium and nitrogen in the bulk of the film were nearly constant over the film thickness, with an average content of ~45 at% and 42 at%, respectively. The quasi-constant concentrations of all elements testify a non-preferential $Ar^+$ sputtering process, contrary to what
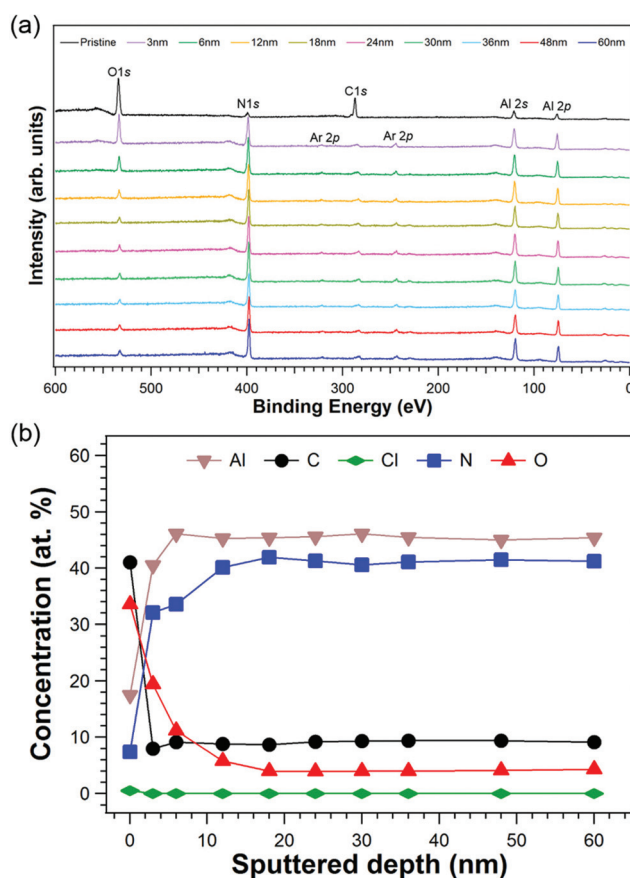
**Fig. 3** (a) XPS survey spectra and (b) atomic concentration in the bulk of the AlN ALD film grown at 450 °C as a function of the depth, deduced from XPS.

was reported for III-nitrides by J. T. Grant *et al.*[37] Concerning other elements, Fig. 4 shows that after the first sputtering cycles, the oxygen concentration decreases exponentially with depth, reaching ~4.0 at% at a depth of ~36 nm, while the carbon content equally decreases with the same depth to ~9.0 at%.

The lower amount of oxygen in the bulk compared to the surface confirms the hypothesis that a significant portion of the surface oxide is resulting from atmospheric oxidation and does not stem from the deposition process itself. The oxygen content in the bulk of the film can be explained by water impurities in the dosed MMH, as this compound is hygroscopic.[38] Furthermore, the presence of oxygen can also be associated with TMA reacting with water impurities during the ALD process.[39] As far as carbon is concerned, its content in the film is not too high, and likely to result from the partial thermal decomposition of TMA.

Fig. 5 shows the XPS spectra of the Al 2p and N 1s core level regions after 20 h of $Ar^+$ sputtering (~60 nm depth). The Al 2p spectrum shows an asymmetric peak, with two components in the fit; the main peak at a binding energy (B.E.) of 74.3 eV is assigned to the Al–N/Al–C bonds, while the other peak located at 75.3 eV can be assigned to the Al–N–O species.[39–41] The Al–N–O feature is generally referred to as aluminium oxynitride
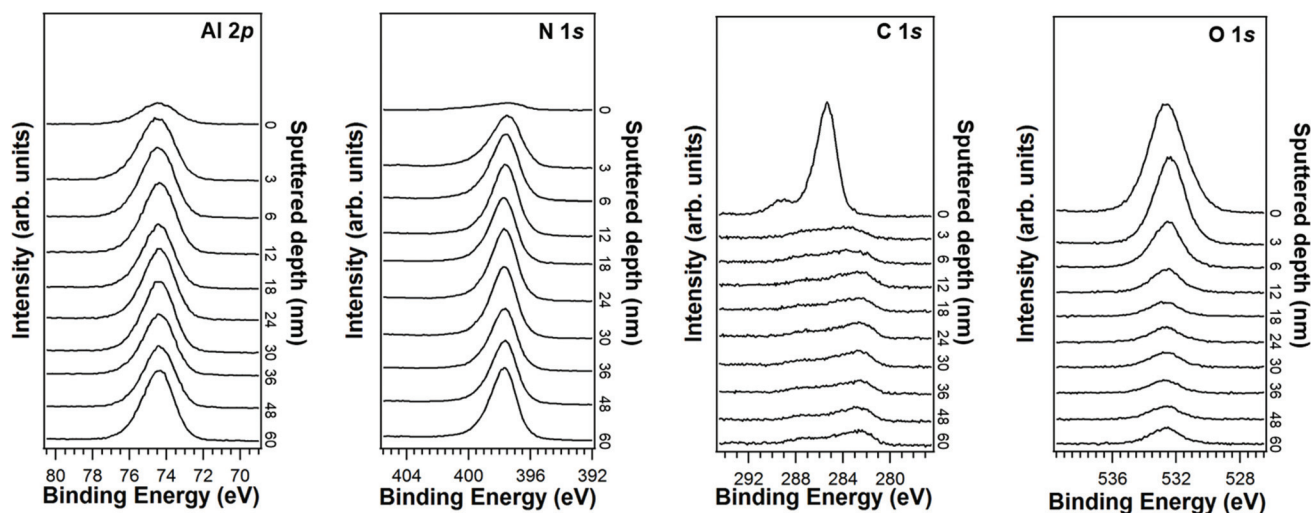
**Fig. 4** XPS spectra of the Al 2p, N 1s, C 1s and O 1s core level regions of the AlN ALD film grown at 450 °C, before and after Ar⁺ sputtering.
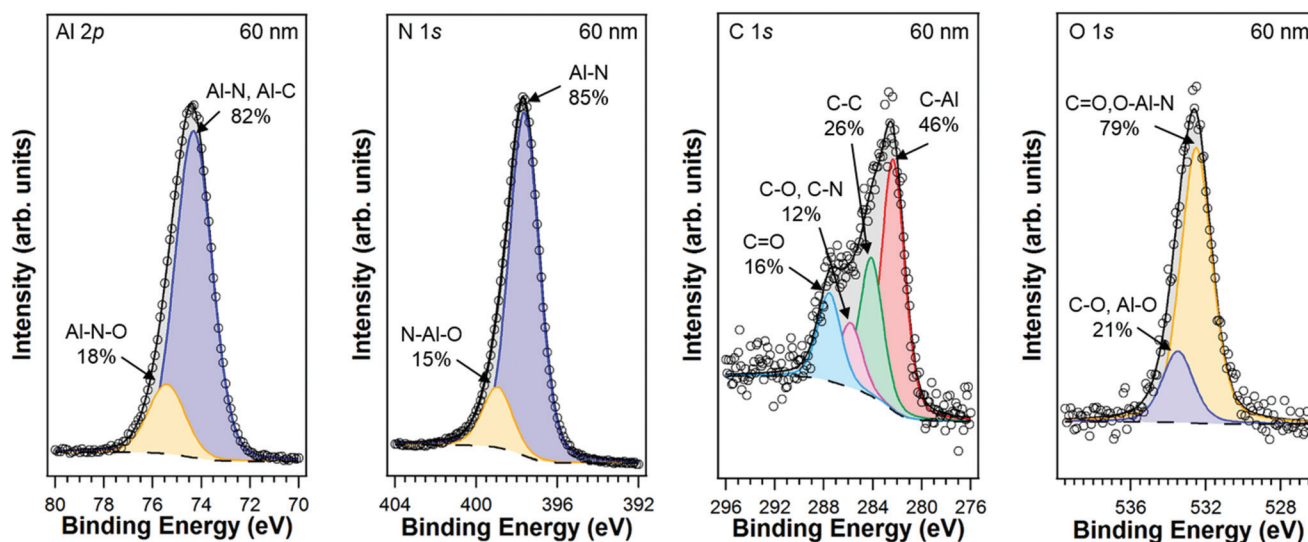


**Fig. 5** XPS spectra of the Al 2p, N 1s, C 1s and O 1s core level regions of a AlN ALD film grown at 450 °C after 20 h of Ar⁺ sputtering.

$(AlO_xN_y)$.[40–42] The asymmetric N 1s peak is the best fitted with two components; the main peak at a B.E. of 397.6 eV corresponds to N–Al bonds, while the other component at 399.0 eV can be ascribed to N–Al–O bonds.[40]

The C 1s spectrum shows an asymmetric peak, which is deconvoluted into four components to obtain a good fit; the main component at a B.E. of 282.3 eV is assigned to C–Al species,[41,43,44] while the other peaks located at 284.1 eV, 285.8 eV and 287.5 eV can be ascribed to C–C, C–O/C–N, and C=O bonds, respectively.[45,46] The asymmetric O 1s spectrum is fitted with two components; the main peak at 532.5 eV corresponds to O–Al–N/C=O bonds, while the other peak at 533.5 eV can be assigned to Al–O/C–O bonds.[40]

Table 1 shows the atomic concentration of elements at various deposition temperatures. Note that the Al/N ratio is

**Table 1** Atomic concentration of elements in AlN films at various deposition temperatures

| Deposition temperature | Element content, at% | | | |
| --- | --- | --- | --- | --- |
| | Al | N | C | O |
| 400 | 46 | 39 | 3 | 12 |
| 425 | 44 | 37 | 7 | 12 |
| 450 | 45 | 42 | 9 | 4 |

almost constant, while the concentrations of carbon and oxygen change noticeably. For example, the concentration of carbon for deposition at 400 °C is 3 times lower than that at 450 °C, which can be explained with the partial thermal decomposition of TMA at high temperatures.

### Mechanical properties

From the nanoindentation theory, which says that the depth of penetration should not exceed 10% of the coating thickness and due to the imperfect geometry of the used indenters, it is generally recommended to perform measurements on coatings with a thickness of more than 100 nm.[47] This may allow one to obtain real values of mechanical properties of the thin films where the superposition of the substrate properties is minimized. Therefore, for the analysis of mechanical properties a thicker AlN film (370 nm) was synthesized at 450 °C.

The obtained values for the mechanical properties of the AlN film (Fig. 6) were supplemented with the results calculated for the bare substrate (denoted as the dashed lines in the graph). The ALD-synthesized AlN films exhibited hardness ($H$) and elastic modulus ($E$) mean values of $13.8 \pm 0.2$ GPa and $164 \pm 1$ GPa, respectively. In the case of the bare substrate its hardness was lower ($12.3 \pm 0.1$ GPa), while the Young's modulus was higher $173 \pm 1$ GPa. The obtained results are slightly lower than those reported in the literature for other ALD-synthesized AlN coatings. They also correlate roughly with the results obtained for plasma-enhanced ALD films deposited at low-temperature ($H$ and $E$ of ~15 and ~160 GPa, respectively), while for high-temperature films the values are higher (~19.5 and ~180 GPa, respectively).[48] These differences may result from the density, the degree of crystallinity, and the impurity levels of the synthesized films. In fact, the AlN films with an amorphous structure usually show lower hardness values as compared to crystalline phases.

This can be attributed to a short-range order of the amorphous films that generally results in lower stiffness (hardness). However, the results of this study are consistent with some of the reports on amorphous AlN produced by other techniques, *e.g.* a beam-assisted filtered cathodic vacuum arc ($H = 11.8$–14.5 GPa), while other papers report twice higher values of hardness (approx. 23 GPa) for the amorphous coatings synthesized by pulsed laser deposition.[49,50] Another study on the mechanical properties of AlN coatings synthesized by magnetron sputtering reports values of hardness and modulus ranging from 10 to 21 GPa, and 120 to 200 GPa, respectively, depending on synthesis conditions (*e.g.* sputtering pressure).[51]

A measure of adhesion strength of the thin film to the substrate is the load at which the total peeling-off of the film from the substrate surface occurs, denoted here as critical load $L_c$. Hardness and elastic modulus are important material parameters that indicate the resistance to elastic/plastic deformation and could be used for the estimation of the coating wear behaviour. The calculation of the elastic strain to failure (which is related to $H/E$) and the resistance to plastic deformation (often associated with $H^3/E^2$) may be translated directly into the behaviour of the film during wear and scratch tests (assuming uniformity of the film).[52,53] Scratch adhesion and wear results of the studied films are presented in Table 2, supplemented with the results of the $H/E$ and $H^3/E^2$ parameters.

The critical load obtained in nanoscratch tests, for the AlN ALD film was approximately 32 mN, a value that can be regarded as relatively high for an adhesion to the substrate. Comparing the results of wear and scratch resistance with the calculated values of $H/E$ and $H^3/E^2$, it can be noticed that the presented correlations are consistent with the literature.[52,53] Most of the failure mechanisms begin with plastic deformation, thus the coating should be more resistant to wear when it has a high resistance to plastic deformation and,

**Table 2** Wear coefficient and scratch critical load of the AlN ALD film, supplemented with the corresponding results of $H/E$ and $H^3/E^2$

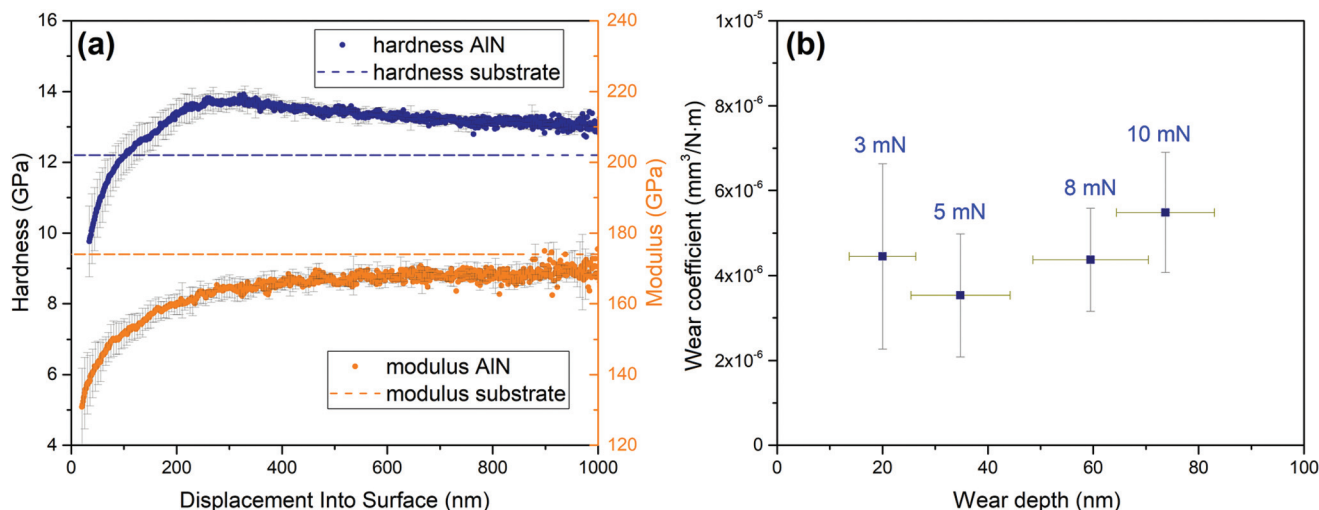| | Wear coefficient ($mm^3\ N^{-1}\ m^{-1}$) | Critical load $L_c$ (mN) | $H/E$ | $H^3/E^2$ (GPa) |
|---|---|---|---|---|
| AlN | $(4.5 \pm 1.6) \times 10^{-6}$ | $32.2 \pm 1.3$ | 0.084 | 0.097 |



**Fig. 6** (a) Hardness and elastic modulus depth profiles of AlN coatings with reference to the bare substrate (dashed lines). (b) Wear coefficient *vs.* depth of the wear track created in the tribological test.

therefore reaches a high value of $H^3/E^2$ ($H/E$). In addition, to analyse whether the films are homogeneous in terms of wear resistance, the reciprocating wear tests were performed for four different loading values (applied wear loads of 3, 5, 8 and 10 mN) which resulted in different depths of the wear tracks at the end of the test. In Fig. 6 the evolution of the wear coefficient as a function of wear load (or wear depth) is depicted. These results confirm a homogeneous wear resistance of the AlN film regardless of the applied wear load, with an average wear coefficient of ~$4.5 \times 10^{-6}$ mm$^3$ N$^{-1}$ m$^{-1}$. A literature survey on the wear resistance of the AlN thin films revealed very few studies performed under similar conditions to those reported in our paper. For instance, the wear test results of the AlN films with various degrees of $c$-axis texturing, obtained by reactive radio-frequency magnetron sputtering were presented.[54] In the case of the AlN film with the highest crystalline quality the wear rate was ~$8.6 \times 10^{-7}$ mm$^3$ N$^{-1}$ m$^{-1}$, while for the film with the lowest crystallinity the wear rate was one order of magnitude higher ~$8.5 \times 10^{-6}$ mm$^3$ N$^{-1}$ m$^{-1}$ which is in good agreement with our results.[54]

## Conclusions

Amorphous AlN films grown from TMA and MMH by ALD were obtained with a growth rate of 0.66 to 1.34 Å per cycle (375–475 °C). Unfortunately, MMH did not allow to decrease the deposition temperature, which is likely due to its transformation in the gas phase. However, the obtained films were investigated by XRD, XPS and microscopy methods, while the mechanical properties were studied by nanoindentation and shown to be of good quality. The films were amorphous and become polycrystalline after annealing at 1000 °C in a nitrogen atmosphere. Through the whole thickness, the Al/N ratio was close to stoichiometry. Depending on the deposition temperature the amount of impurities varied from 3 to 9 at% for carbon, and 4 to 12 at% for oxygen. The values of mechanical characteristics of the studied films were ~14 GPa (hardness) and ~164 GPa (Young's modulus), which are comparable to those of AlN films deposited by other techniques.

## Conflicts of interest

There are no conflicts to declare.

## Acknowledgements

## References

1 J. H. Lu and B. Y. Chen, *J. Vac. Sci. Technol., A*, 2014, **32**, 02B106.

2 Y. Y. Wang, M. S. Wong, W. J. Chia, J. Rechner and W. D. Sproul, *J. Vac. Sci. Technol., A*, 1998, **16**, 3341.

3 E. Osterlund, J. Kinnunen, V. Rontu, A. Torkkeli and M. Paulasto-Krockel, *J. Alloys Compd.*, 2019, **772**, 306.

4 G. Nie, P. Sheng, Y. Li, F. Zuo, Y. Bao and S. Wu, *Int. J. Appl. Ceram. Technol.*, 2021, **18**, 1255.

5 A. Ullah, M. Usman, W. Qingyu, I. Ahmad, R. Y. Khosa and M. Maqbool, *Radiat. Phys. Chem.*, 2021, **180**, 109234.

6 R. K. Choudhary, P. Mishra and R. C. Hubli, *Surf. Eng.*, 2016, **32**, 304.

7 Ch. Fei, X. Liu, B. Zhu, D. Li, X. Yang, Y. Yang and Q. Zhou, *Nano Energy*, 2018, **51**, 146.

8 S. Zhao, A. T. Connie, M. H. T. Dastjerdi, X. H. Kong, Q. Wang, M. Djavid, S. Sadaf, X. D. Liu, I. Shih, H. Guo and Z. M, *Sci. Rep.*, 2015, **5**, 8332.

9 A. G. Baca, A. M. Armstrong, A. A. Allerman, E. A. Douglas, C. A. Sanchez, M. P. King, M. E. Coltrin, T. R. Fortune and R. J. Kaplar, *Appl. Phys. Lett.*, 2016, **109**, 033509.

10 A. Adikimenakis, K. E. Aretouli, E. Iliopoulos, A. Kostopoulos, K. Tsagaraki, G. Konstantinidis and A. Georgakilas, *Microelectron. Eng.*, 2009, **86**, 1071.

11 D. D. Koleske, J. J. Figiel, D. L. Alliman, B. P. Gunning, J. M. Kempisty, J. R. Creighton, A. Mishima and K. Ikenaga, *Appl. Phys. Lett.*, 2017, **110**, 232102.

12 L. Huang, X.-D. Wang, K. W. Hipps, U. Mazur, R. Heffron and J. T. Dickinson, *Thin Solid Films*, 1996, **279**, 43.

13 D. Solonenko, C. Schmidt, C. Stoeckel, K. Hiller and D. R. T. Zahn, *Phys. Status Solidi B*, 2020, **257**, 1900400.

14 V. Brien and P. Pigeat, *J. Cryst. Growth*, 2007, **299**, 189.

15 Y. Zhao, X. Peng, T. Fu, Ch. Huang, H. Xiang, N. Hu and Ch. Yan, *Materialia*, 2018, **2**, 148.

16 H. Oikawa, R. Akiyama, K. Kanazawa, S. Kuroda, I. Harayama, K. Nagashima, D. Sekiba, Y. Ashizawa, A. Tsukamoto, K. Nakagawa and N. Ota, *Thin Solid Films*, 2015, **574**, 110.

17 P. Vashishta, R. K. Kalia, A. Nakano and J. P. Rino, Collaboratory for Advanced Computing and Simulations, *J. Appl. Phys.*, 2011, **109**, 033514.

18 D. Riihelä, M. Ritala, R. Matero, M. Leskelä, J. Jokinen and P. Haussalo, *Chem. Vap. Deposition*, 1996, **2**, 277.

19 P. Rouf, P. Sukkaew, L. Ojamäe and H. Pedersen, *J. Phys. Chem. C*, 2020, **124**, 14176.

20 R. Dallaev, D. Sobola, P. Tofel, L. Škvarenina and P. Sedlák, *Coatings*, 2020, **10**, 954.

21 H. Altuntas and T. Bayrak, *Electron. Mater. Lett.*, 2017, **13**, 114.

22 S. Banerjee, A. A. I. Aarnink, R. van de Kruijs, A. Y. Kovalgin and J. Schmitz, *Phys. Status Solidi C*, 2015, **12**, 1036.

23 H. Seppänen, I. Kim, J. Etula, E. Ubyivovk, A. Bouravleuv and H. Lipsanen, *Materials*, 2019, **12**, 406.

24 W.-C. Kao, W.-H. Lee, S.-H. Yi, T.-H. Shen, H.-C. Lin and M.-J. Chen, *RSC Adv.*, 2019, **9**, 12226.

25 P. Motamedi and K. Cadien, *J. Cryst. Growth*, 2015, **421**, 452.

26 V. Rontu, P. Sippola, M. Broas, G. Ross, T. Sajavaara, H. Lipsanen, M. Paulasto-Kröckel and S. Franssila, *J. Vac. Sci. Technol., A*, 2018, **36**, 021508.

27 Z. Chen, Z. Zhu, K. Härkönen and E. Salmi, *J. Vac. Sci. Technol., A*, 2019, **37**, 020925.

28 M. Juppo, Mi. Ritala and M. Leskelä, *J. Electrochem. Soc.*, 2000, **147**, 3377.

29 C. C. Wang, M. C. Chiu, M. H. Shiao and F. S. Shieu, *J. Electrochem. Soc.*, 2004, **151**, F252.

30 G. M. Pharr, W. C. Oliver and F. R. Brotzen, *J. Mater. Res.*, 1992, **7**, 613.

31 D. de Faoite, D. J. Browne, F. R. Chang-Díaz and K. T. Stanton, *J. Matter. Sci.*, 2012, **47**, 4211.

32 J. F. Archard, *J. Appl. Phys.*, 1953, **24**, 981.

33 Y. C. Jung, S. M. Hwang, D. N. Le, A. L. N. Kondusamy, J. Mohan, S. W. Kim, J. H. Kim, A. T. Lucero, A. Ravichandran, H. S. Kim, S. J. Kim, R. Choi, J. Ahn, D. Alvarez, J. Spiegelman and J. Kim, *Materials*, 2020, **13**, 3387.

34 I. J. Eberstein and I. Glassman, *Symp. (Int.) Combust., [Proc.]*, 1965, **10**, 365.

35 J. Jokinen, P. Haussalo, J. Keinonen, M. Ritala, D. Riihelä and M. Leskelä, *Thin Solid Films*, 1996, **289**, 159.

36 F. Jose, R. Ramaseshan, S. Dash, S. Bera, A. K. Tyagi and B. Raj, *J. Phys. D: Appl. Phys.*, 2010, **43**, 075304.

37 J. T. Grant, *J. Surf. Anal.*, 2006, **13**, 166.

38 E. W. Schmidt, *Hydrazine and Its Derivatives: Preparation, Properties, Applications, 2 Volume Set*, Wiley-Interscience, New York, Chichester, Weinheim, Brisbane, Singapore, and Toronto, 2001.

39 J. Zhang, Q. Zhang, H. Yang, H. Wu, J. Zhou and L. Hu, *Appl. Surf. Sci.*, 2014, **315**, 110.

40 L. Rosenberger, R. Baird, E. McCullen, G. Auner and G. Shreve, *Surf. Interface Anal.*, 2008, **40**, 1254.

41 C. Hinnen, D. Imbert, J. M. Siffre and P. Marcus, *Appl. Surf. Sci.*, 1994, **78**, 219.

42 M. Alevli, C. Ozgit, I. Donmez and N. Biyikli, *Phys. Status Solidi A*, 2012, **209**, 266.

43 J. Xiang, Y. Ding, L. Du, C. Xu, T. Li, X. Wang, J. Li and C. Zhao, *ECS J. Solid State Sci. Technol.*, 2016, **5**, P299.

44 A. Zameshin, M. Popov, V. Medvedev, S. Perfilov, R. Lomakin, S. Buga, V. Denisov, A. Kirichenko, E. Skryleva, E. Tatyanin, V. Aksenenkov and V. Blank, *Appl. Phys. A*, 2012, **107**, 863.

45 K. Spyrou, M. Calvaresi, E. K. Diamanti, T. Tsoufis, D. Gournis, P. Rudolf and F. Zerbetto, *Adv. Funct. Mater.*, 2015, **25**, 263.

46 Y. Bourlier, M. Bouttemy, O. Patard, P. Gamarra, S. Piotrowicz, J. Vigneron, R. Aubry, S. Delage and A. Etcheberry, *ECS J. Solid State Sci. Technol.*, 2018, **7**, P329.

47 X. Li and B. Bhushan, *Mater. Charact.*, 2002, **48**, 11.

48 P. Sippola, A. P. Perros, O. M. E. Ylivaara, H. Ronkainen, J. Julin, X. Liu, T. Sajavaara, J. Etula, H. Lipsanen and R. L. Puurunen, *J. Vac. Sci. Technol., A*, 2018, **36**, 051508.

49 X. H. Ji, S. P. Lau, G. Q. Yu, W. H. Zhong and B. K. Tay, *J. Phys. D: Appl. Phys.*, 2004, **37**, 1472.

50 L. Kolaklieva, V. Chitanov, A. Szekeres, K. Antonova, P. Terziyska, Z. Fogarassy, P. Petrik, I. N. Mihailescu and L. Duta, *Coatings*, 2019, **9**, 195.

51 Q. Wei, X. Zhang, D. Liu, L. Jie, K. Zhou, D. Zhang and Z. Yu, *Trans. Nonferrous Met. Soc. China*, 2014, **24**, 2845.

52 A. Leyland and A. Matthews, *Wear*, 2000, **246**, 1.

53 J. Musil, F. Kunc, H. Zeman and H. Poláková, *Surf. Coatings Technol.*, 2002, **154**, 304.

54 C. Besleaga, V. Dumitru, L. M. Trinca, A.-C. Popa, C.-C. Negrila, Ł. Kołodziejczyk, C.-R. Luculescu, G.-C. Ionescu, R.-G. Ripeanu, A. Vladescu and G. E. Stan, *Nanomaterials*, 2017, **7**, 394.